Electronic Supplementary Material (ESI) for Chemical Science.

Supporting Information

Breaking the trade-off between capacity and stability in vanadium-based zinc-ion batteries

Weikang Jiang,[a,b] Kaiyue Zhu,*[b,c] Weili Xie,[b,c] Zhengsen Wang,[b,d] Zuqiao Ou,[b,c] Weishen Yang,*[a,b,c,d]

[a] Department of Chemical Physics, University of Science and Technology of China, Anhui 230026, Hefei, China.

[b] State Key Laboratory of Catalysis, Dalian Institute of Chemical Physics, Chinese Academy of Sciences, Dalian, 116023, China.

[c] University of Chinese Academy of Sciences, Beijing, 100049, China.

[d] School of Chemistry, Dalian University of Technology, Dalian, 116024, China.

E-mail: yangws@dicp.ac.cn (W. Yang); zky218@dicp.ac.cn (K. Zhu)

1. Synthesis of cathode materials

Synthesis of $(NH_4)_{0.5}V_2O_5\cdot 0.5H_2O$ *(NVO)*

$(NH_4)_{0.5}V_2O_5\cdot 0.5H_2O$ (NVO) was prepared via a hydrothermal method. In a typical procedure, certain amounts of NH_4VO_3 (0.585 g) and $H_2C_2O_4$ (0.63 g) were added to deionized (DI) water under vigorous stirring for 30 minutes. The mixture was subsequently loaded into a stainless-steel autoclave with a Teflon liner and held at 130°C for 12 h. After cooling to room temperature naturally, the products were collected and washed with deionized water and absolute ethanol 3 times. The final NVO powders were obtained after drying at 60 ℃ for 12 h in air.

2. Materials Characterization

Phase and microstructure determination

X-ray diffraction (XRD) patterns of the samples were collected using a Rigaku D/MAX-2500/PC with Cu Kα radiation (λ=1.54 Å at 40 kV and 200 mA). The data were recorded from 5° to 60° with an interval of 0.02° and a scan speed of 5°/min. The morphologies of the samples were captured with an FEI Quanta 200 F.

Thermal analysis.

Thermogravimetric analysis (TGA) was performed using a Pyris Diamond TG/DTA. Specimens were placed in an Al_2O_3 crucible with a lid, and TGA data were recorded under air with a flow rate of 50 mL min^{-1} while ramping from room temperature to 600°C at a rate of 5°C min^{-1} and then cooling naturally to room temperature.

Surface chemistry.

The surface chemical compositions and oxidation states of the elements were analysed using a Thermo Fisher Escalab 250 Xi+ spectrometer with Al Ka X-ray radiation (hν=1486.6 eV). Prior to these analyses, the soaked and cycled electrodes were washed thoroughly with DI water to remove electrolyte residue and then dried in a glove box. All the binding energies were corrected by adventitious C 1 s at 284.6 eV.

Properties of the electrolytes

The infrared spectra were obtained using a Nicolet 6700 Fourier transform infrared spectroscopy-attenuated total reflection (FTIR-ATR) spectrophotometer. NV-vis spectrophotometry was conducted on a Shimadzu UV-1900 spectrophotometer.

3. Electrochemical Characterization

Ionic conductivity of the electrolyte

The ionic conductivities of 1 M $Zn(OTf)_2$ electrolytes utilizing AN with various H2O contents as solvents were measured by a portable conductivity meter (DDBJ-350F).

Battery cell assembly

Electrochemical tests were carried out on CR2032-type coin cells. To prepare the cathode, 60 wt% active materials, 26 wt% Super-P, and 14 wt% polyvinylidene fluoride (PVDF) were thoroughly mixed and dispersed into N-methyl pyrrolidone (NMP). The resultant slurry was then coated uniformly onto a 14 mm diameter stainless steel mesh (SSM), resulting in ~ 1 mg cm^{-2} and ~13 mg cm^{-2} active mass loading, followed by drying at 60°C for 12 h. In a full ZIB cell, zinc foil was used as the anode, NVO was used as the cathode, and glass microfiber filters (Whatman, Grade GF/A) were used as the separator. $Zn(OTf)_2$ powders were dissolved in acetonitrile (AN) with various water contents (0%, 5%, 8%, 15%, 100%) to form 1 M solutions. For clarity, electrolytes of 1 M $Zn(OTf)_2$ in pure AN, AN containing 5% H_2O, AN containing 8% H_2O, AN containing 15% H_2O, AN containing 30% H_2O, AN containing 50% H_2O, and pure H_2O are denoted as E-0% H_2O, E-8% H_2O, E-15% H_2O, E-30% H_2O, E-50% H_2O, and E-100% H_2O, respectively. Similarly, electrolytes of 1 M $Zn(OTf)_2$ in pure DMF, DMF containing 8% H_2O, and DNF containing 20% H_2O are denoted as E-0% H_2O/DMF, E-8% H_2O/DMF, and E-20% H_2O/DMF, respectively. Electrolytes of 1 M $Zn(OTf)_2$ in pure methanol (MEOH), MEOH containing 8% H_2O, MEOH containing 15% H_2O, MEOH containing 40% H_2O, and MEOH containing 60% H_2O are denoted as E-0% H_2O/MEOH, E-8% H_2O/MEOH, E-15% H_2O/MEOH, E-40% H_2O/MEOH, and E-60% H_2O/MEOH, respectively.

Electrochemical testing

The CR2032-type coin cells were assembled in air and tested using a LAND battery testing system (CT2001A) within a potential window of 0.2-1.6 V (*vs* Zn/Zn^{2+}). Cyclic voltammetry (CV) was conducted in a three-electrode configuration with the working electrode (WE) of the NVO cathode on a Princeton PARSTAT electrochemical workstation. A Zn ring and Zn plate were used as the reference and counter electrodes, respectively. Electrochemical impedance spectroscopy (EIS) was performed in a three-electrode configuration on a Princeton PARSTAT electrochemical working station over the frequency range from 0.1 to 100 kHz with a perturbation amplitude of 10 mV. The galvanostatic intermittent titration technique was employed to determine the ion diffusivity using a series of galvanostatic discharge pulses of 10 min at 100 mA g^{-1}, followed by a 1 h relaxation process. The ion diffusion coefficient (D_{ion}^{GITT}) was calculated as follows:[1]

$$D_{ion}{}^{GITT} = \frac{4L^2}{\pi\tau}\left(\frac{\Delta E_s}{\Delta E_t}\right)^2 \tag{S1}$$

where τ is the constant current pulse time; L corresponds to the ion diffusion length, which is equal to the thickness of the electrode; ΔEs is the change in steady-state voltage during a single-step GITT experiment; and ΔEt is the change in cell voltage at a constant current minus IR loss during each galvanic step.

4. **Theoretical calculations**

The optimization of the molecules was carried out using the Gaussian16 software package, where density functional theory (DFT) with the B3LYP hybrid exchange-correlation functional was employed.[2-4] The 6-311+G(d, p) basis set was adopted for all the DFT calculations.[5,6]

For molecular dynamics (MD) simulations, the GROMACS package with the Amber03 force field was utilized.[7,8] Water molecules were simulated using the OPC model,[9] while the MD parameters for Zn^{2+} were within the in-built force field parameters. The MD parameters for acetonitrile molecules were generated by Sobtop[10,] and the corresponding atom charges were based on RESP charges.[11] The MD parameters for $CF_3SO_3^-$ were obtained from the literature. The simulation system consisted of 60 Zn^{2+} and 120 $CF_3SO_3^-$ ions in a $4.5\times4.5\times4.5$ nm^3 box. To ensure system equilibrium, an NVT run was performed at 298.15 K for 1.2 ns, followed by an NPT run at 298.15 K for 50 ns. The radial distribution functions (RDFs) were calculated using the built-in module in the GROMACS package.

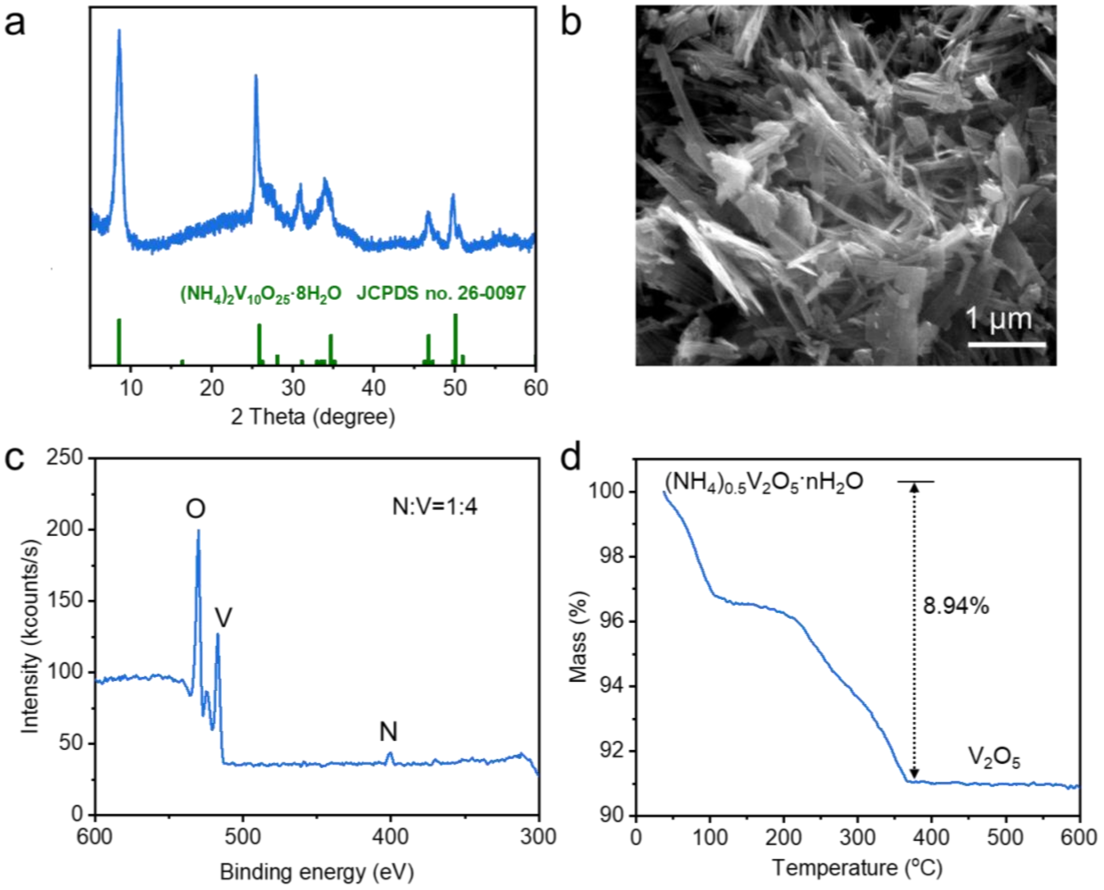

Fig. S1 (a) XRD pattern, (b) SEM image, (c) XPS spectrum, and (d) thermogravimetric analysis under an air atmosphere for the as-prepared $(NH_4)_{0.5}V_2O_5{\cdot}0.5H_2O$ (NVO) powders.

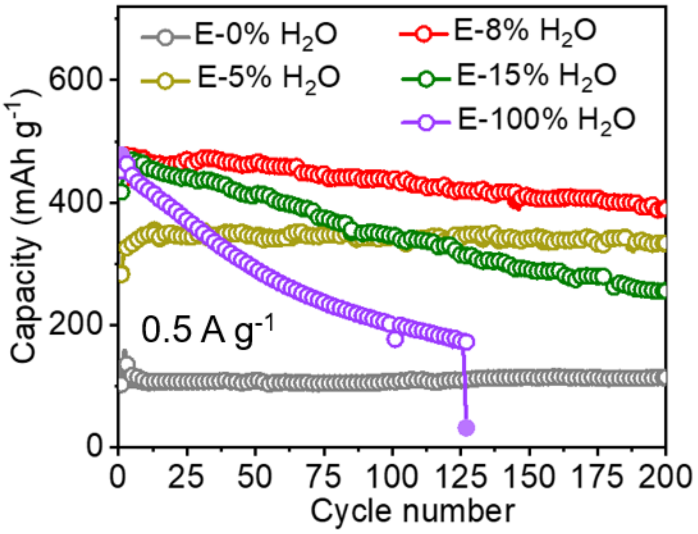

Fig. S2 Cycling performance at 0.5 A g^{-1} of Zn||NVO in electrolytes with various water contents.

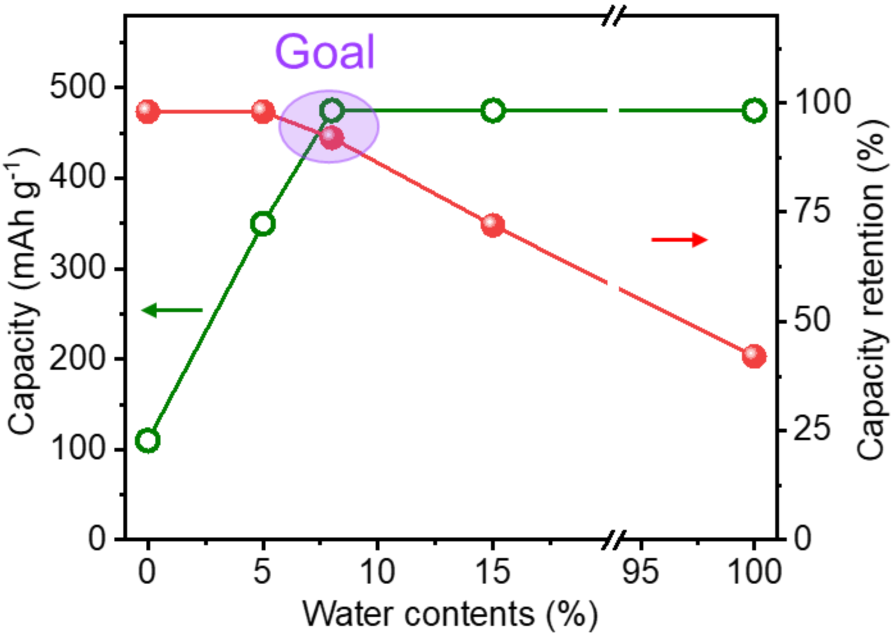

Fig. S3 Capacity and capacity retention after 100 cycles at 0.5 A g^{-1} for Zn||NVO cells in 1 M $Zn(OTf)_2$ using AN with various water contents as solvents.

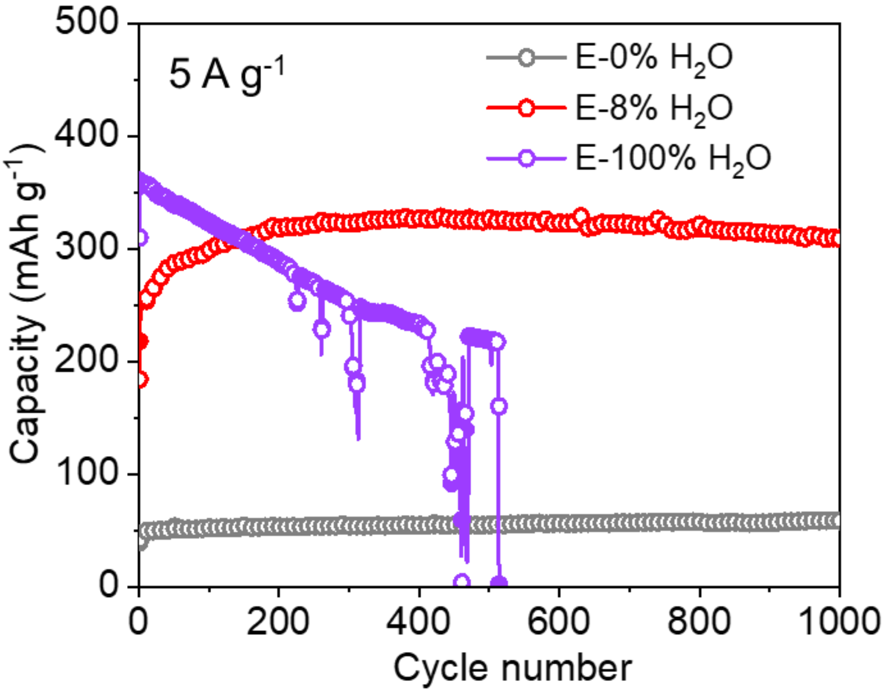

Fig. S4 Cycling performance of Zn||NVO at 5 A g^{-1} in 1 M $Zn(OTf)_2$ using AN solvents with various H_2O contents.

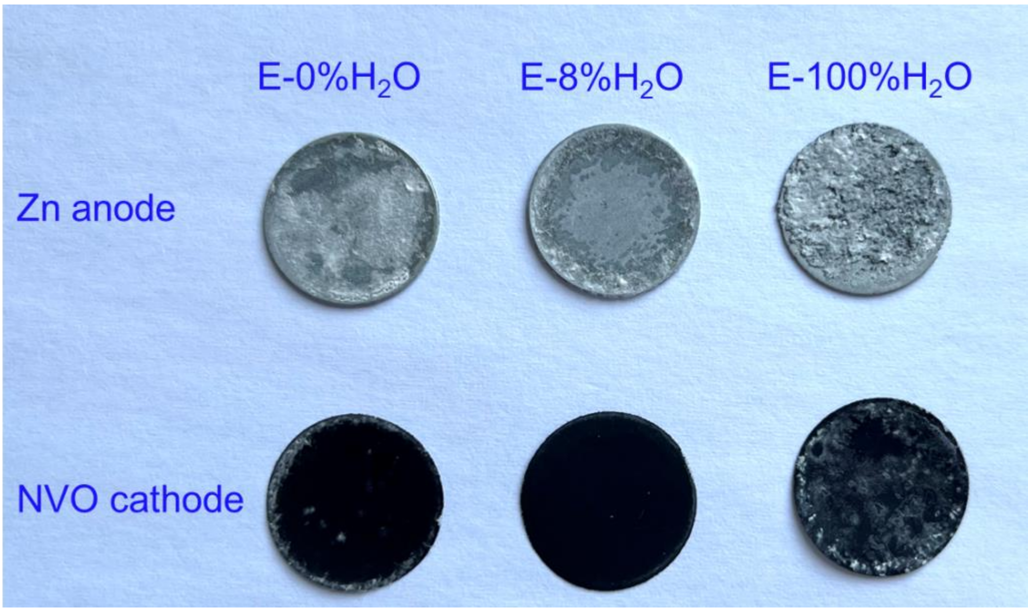

Fig. S5 Photographs of Zn anodes and NVO cathodes after 100 cycles at 0.5 A g^{-1} in 1 M $Zn(OTf)_2$ electrolyte using acetonitrile (AN) with various water contents, such as pure AN (E-0% H_2O), a H_2O content of 8% (E-8% H_2O), and pure water (E-100% H_2O).

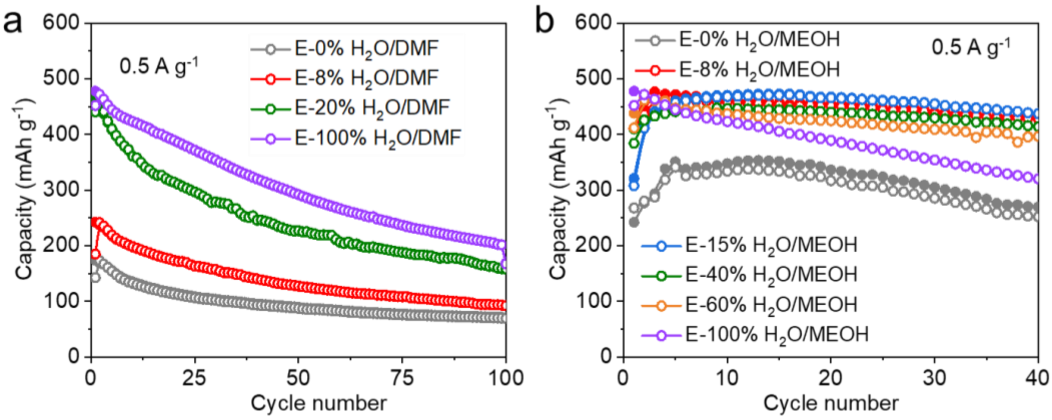

Fig. S6 (a) Cycling performance at 0.5 A g^{-1} of Zn||NVO in 1 M $Zn(OTf)_2$ using dimethylformamide (DMF) solvent with various H_2O contents. (b) Cycling performance at 0.5 A g^{-1} of Zn||NVO in 1 M $Zn(OTf)_2$ using methanol (MEOH) as the solvent with various H_2O contents.

Similarly, the water content in electrolytes using other solvents (DMF, MEOH) strongly impacts the capacity and stability of zinc-ion batteries.

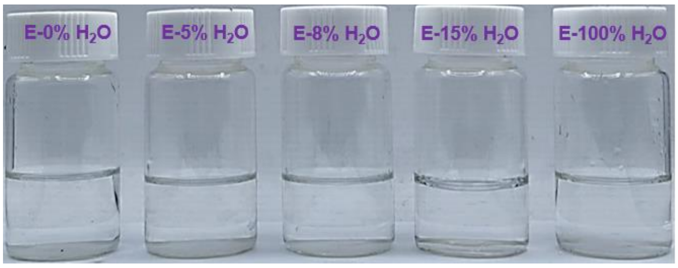

Fig. S7 Optical images of $Zn(OTf)_2$ electrolytes with various water contents (E-0% H_2O, E-5% H_2O, E-8% H_2O, E-15% H_2O, E-100% H_2O).

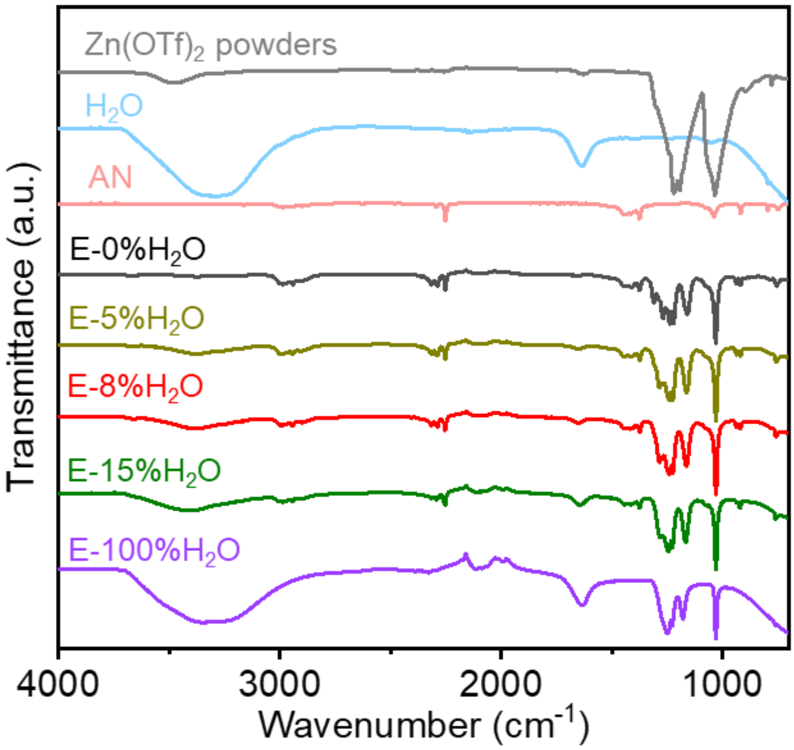

Fig. S8 FT-IR spectra of $Zn(OTf)_2$ powders and water, AN, and $Zn(OTf)_2$ electrolytes in AN with various H_2O contents.

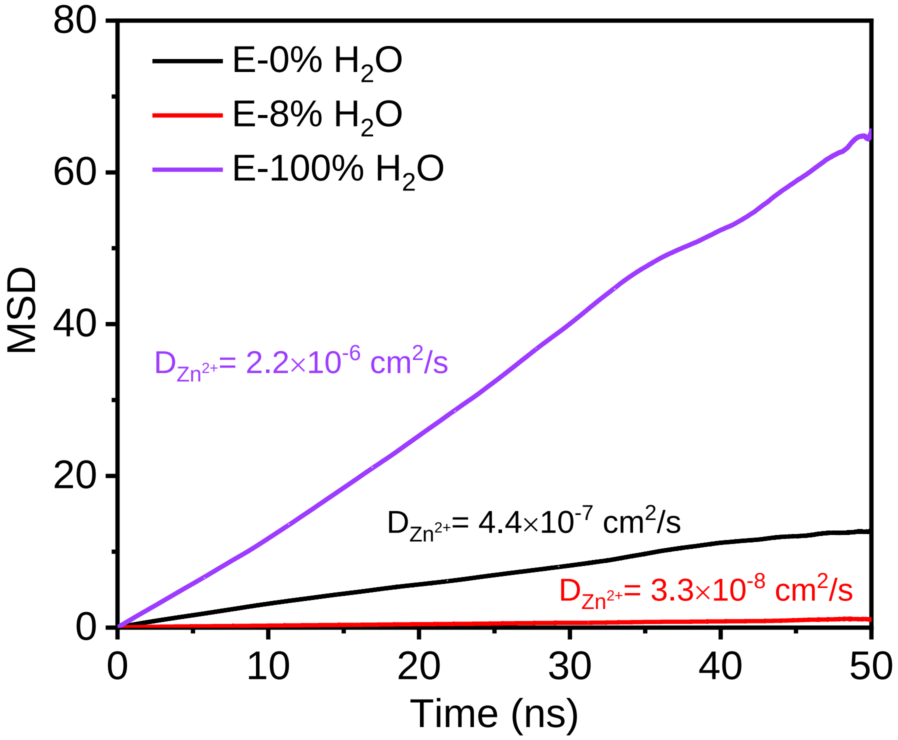

Fig. S9 Mean squared displacement (MSD) of Zn^{2+} in 1 M $Zn(OTf)_2$ electrolyte using AN with various water contents.

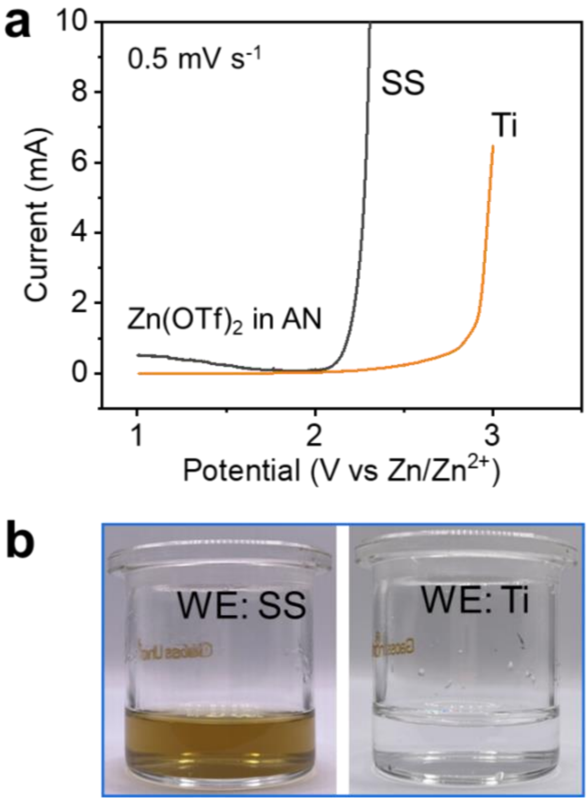

Fig. S10 (a) Linear sweep voltammetry (LSV) curves in E-0% H_2O using stainless steel (SS) and Ti as working electrodes (WEs). (Counter electrode (CE): Zn foil; reference electrode (CE): Zn foil). (b) Photographs of electrolytes after LSV curves.

The observed easy oxidation in the E-0% H_2O electrolyte is likely a consequence of stainless steel (SS) oxidation in AN-based electrolytes. As shown in Fig. S10a, there is a significant increase in the onset potential for oxidation when the working electrode is changed from SS to Ti. This can be attributed to the leaching of Ni and Fe from the SS, leading to their oxidation. Furthermore, Fig. S10b provides clear evidence that the E-0% H_2O electrolyte changes color from colorless to brown after linear sweep voltammetry (LSV) is performed using SS as the working electrode, while the E-0% H_2O electrolyte remains colorless after LSV using Ti as the working electrode. This difference in color change is likely due to the instability of SS.

It is important to note that Zn-ion batteries (ZIBs) are commonly assembled in 2032 coin cells made of stainless steel. Therefore, we measured the electrochemical stability windows of the electrolytes using SS as the working electrode.

By adding a certain amount of water to AN, the leaching of ions from SS can be mitigated, resulting in a higher onset potential for oxidation. However, when the water content is increased to a higher level (E-100% H_2O), water oxidation occurs more easily than when the water content is increased to E-8% H_2O.

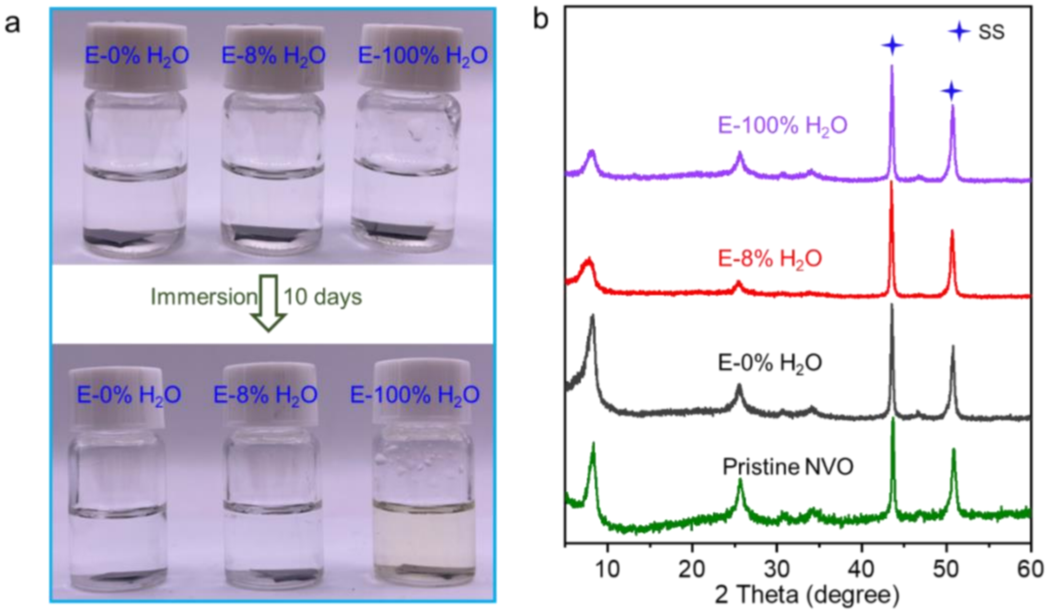

Fig. S11 Optical images of NVO cathodes in 1 M $Zn(OTf)_2$ using AN solvent with various H_2O contents (E-0% H_2O, E-8% H_2O, E-100% H_2O) in the pristine state and after immersion for 10 days. (b) XRD patterns of the NVO cathode after immersion in various electrolytes for 10 days.

Notably, Fig. S11a shows that the soaking solution (E-0% H_2O and E-8% H_2O) is still colorless during soaking NVO, indicating no V dissolution in the solution. In contrast, the color changes from colorless to pale yellow during soaking NVO in E-100% H_2O, suggesting V-dissolution. Therefore, decreasing the water content in the electrolytes could mitigate vanadium dissolution.

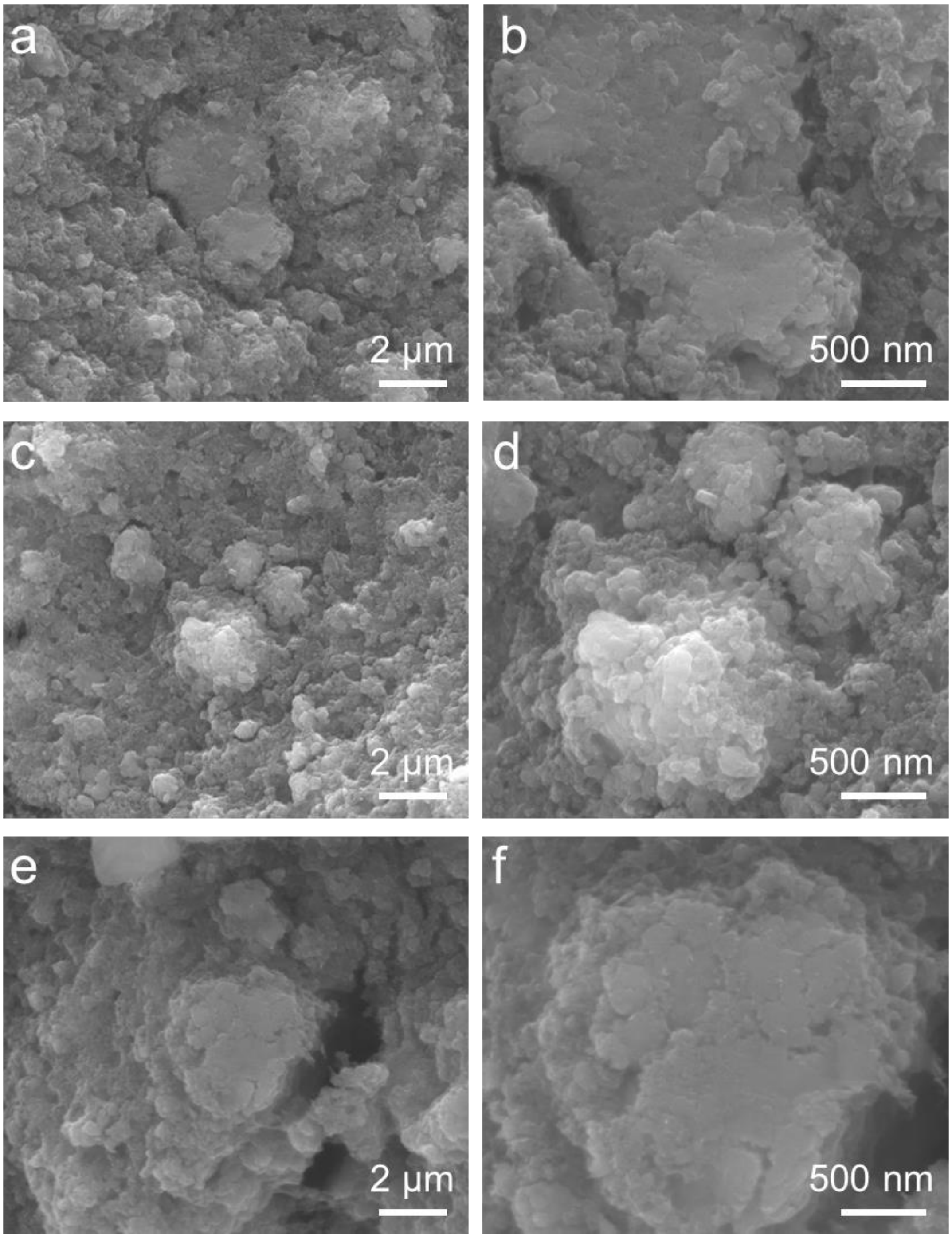

Fig. S12 SEM images of the NVO cathode after immersion in various electrolytes for 10 days: (a, b) E-0% H_2O, (c, d) E-8% H_2O, and (e, f) E-100% H_2O.

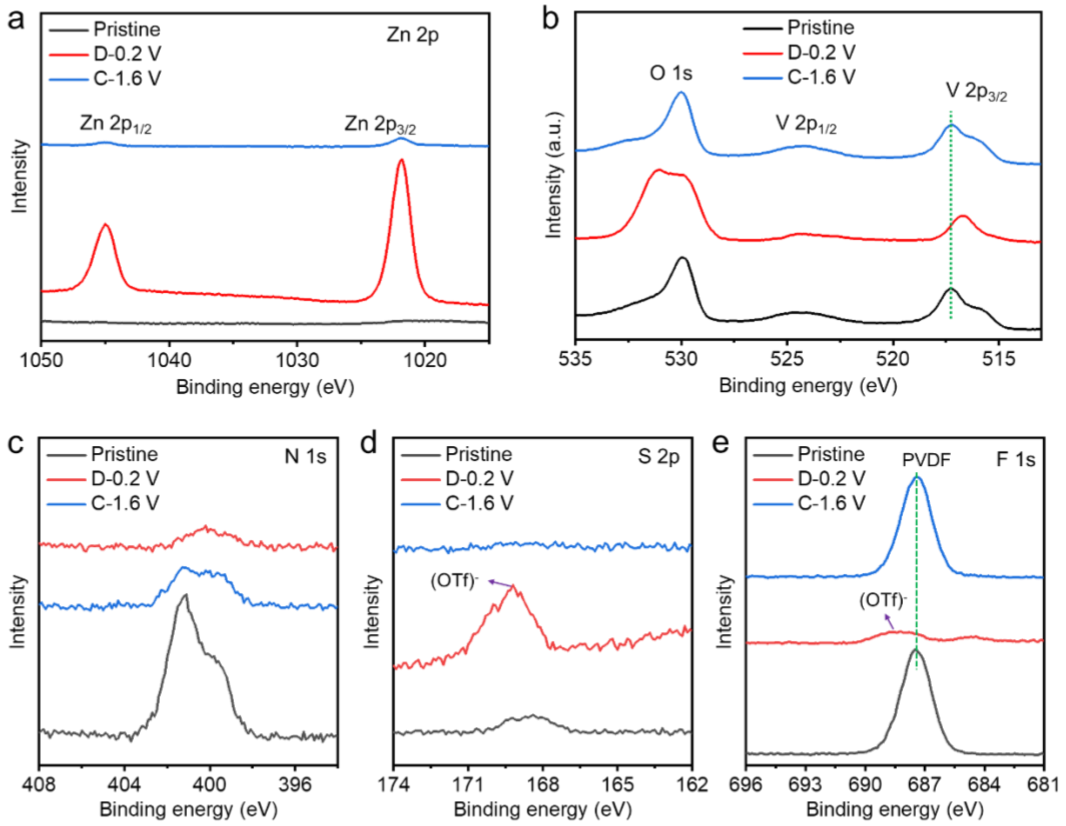

Fig. S13 (a) Zn-2p, (b) O-1s and V-2p, (c) N-1s XPS, (d) S-2p, and (e) F-1s spectra of NVO cathodes in the pristine state, discharged state (D-0.2 V) and charged state (C-1.6 V) in E-8% H_2O.

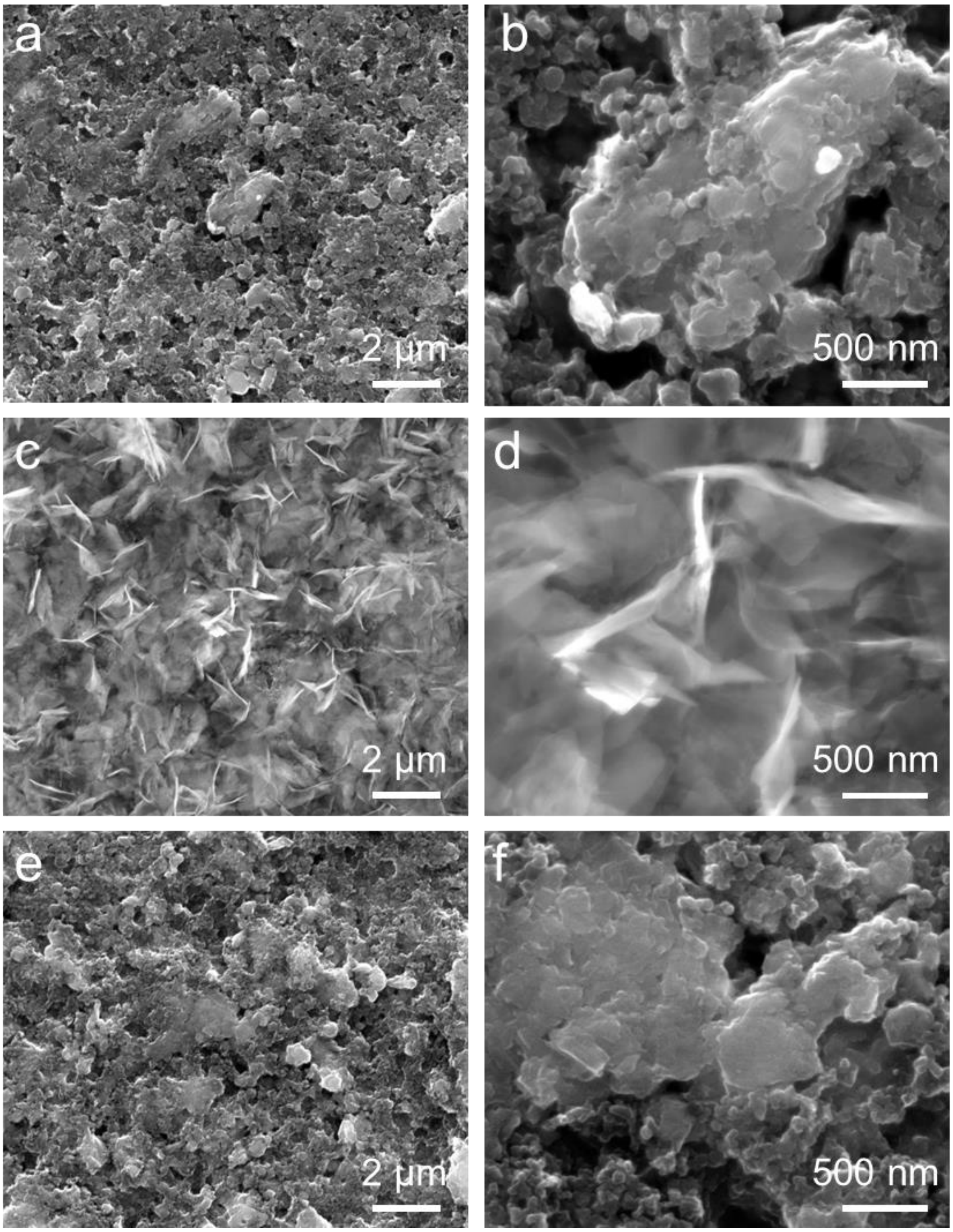

Fig. S14 SEM images of NVO cathodes in the (a, b) pristine state, (c, d) discharged state (D-0.2 V) and (e, f) charged state (C-1.6 V) in E-8% H_2O.

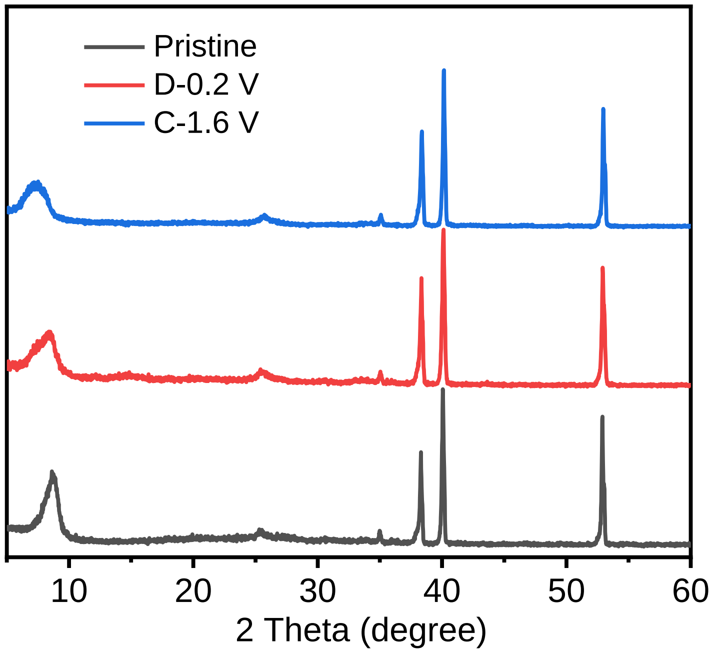

Fig. S15 XRD patterns of NVO cathodes in the pristine state, discharged state (D-0.2 V) and charged state (C-1.6 V) in E-8% H_2O.

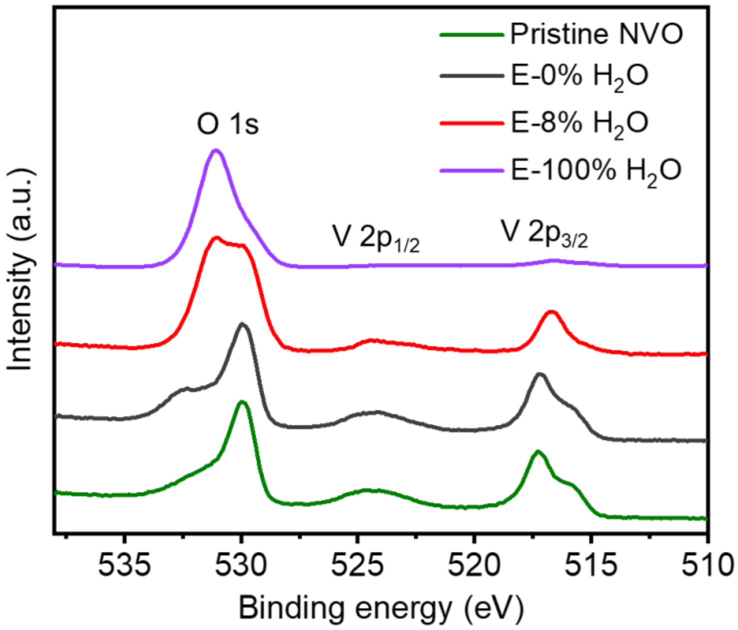

Fig. S16 O-1s and V-2p XPS spectra of the NVO cathode in the discharged state in electrolytes with various water contents.

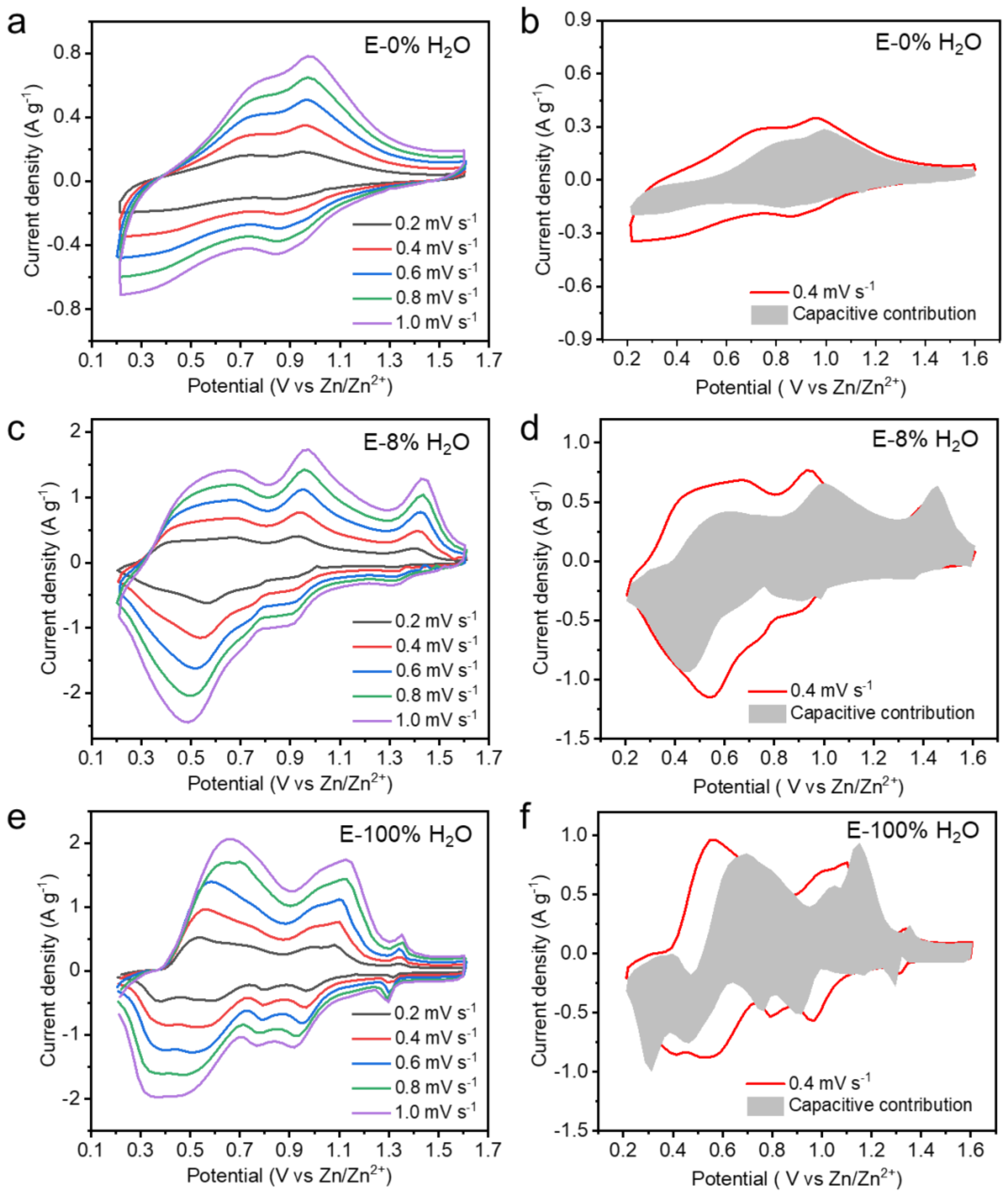

Fig. S17 CV curves at various scan rates and capacitive contributions (gray portion) and diffusion contributions (white portion) of NVO in the three-electrode cell (WE: NVO, CE: Zn plate, RE: Zn ring) using various electrolytes: (a, b) E-0% H_2O, (c, d) E-8% H_2O, and (e, f) E-100% H_2O.

In general, the current (i) of a CV of a battery obeys the power-law relationship with the scan rate (ν) as follows:[12-14]

$$i = k_1\nu + k_2\nu^{1/2} \tag{S2}$$

where $k_1\nu$ and $and\ k_2\nu^{1/2}$ represent the capacitive and diffusion contributions, respectively.

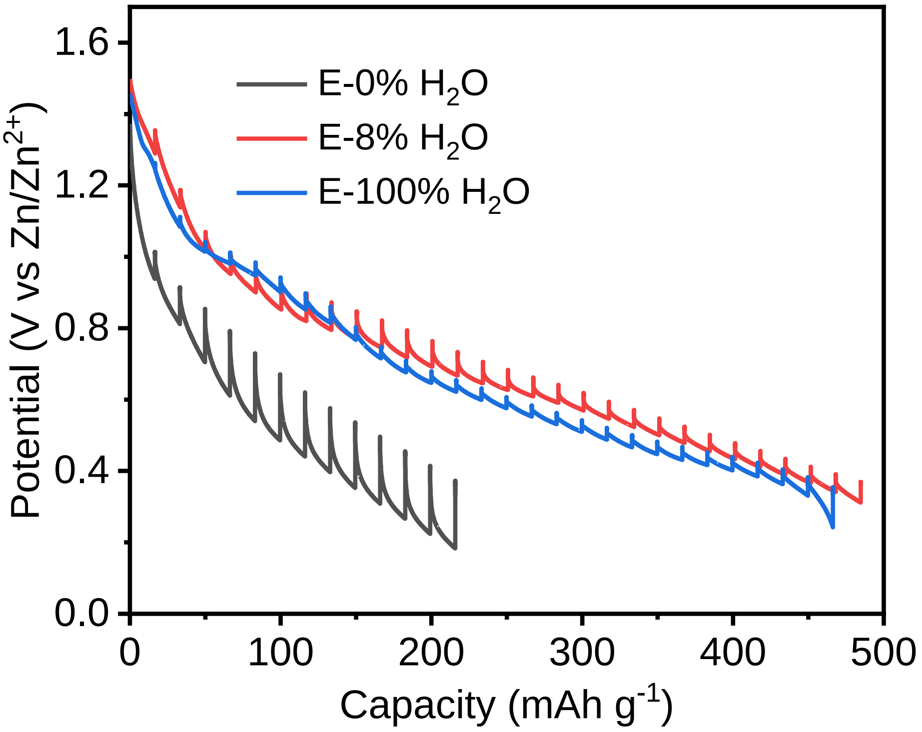

Fig. S18 Discharge GITT curves at 0.1 A g^{-1} for the Zn||NVO cell in electrolytes with various water contents.

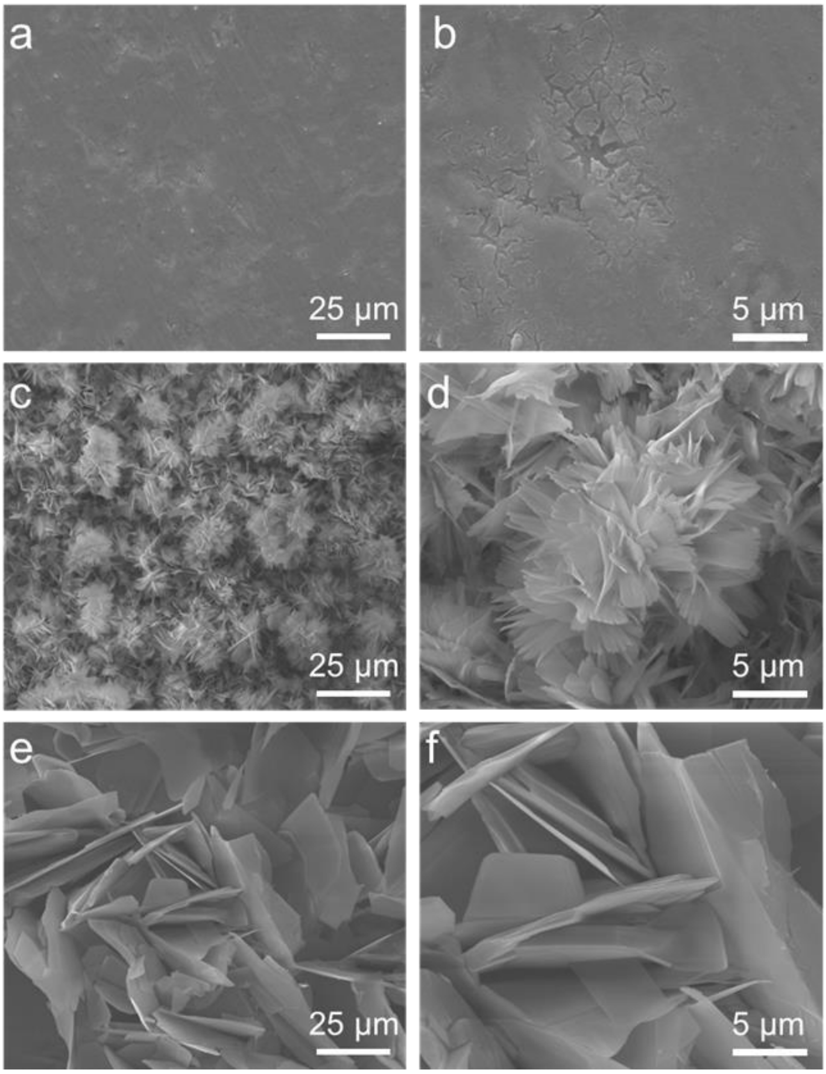

Fig. S19 SEM images of the Zn anode after immersion in various electrolytes for 10 days: (a, b) E-0% H_2O, (c, d) E-8% H_2O, and (e, f) E-100% H_2O.

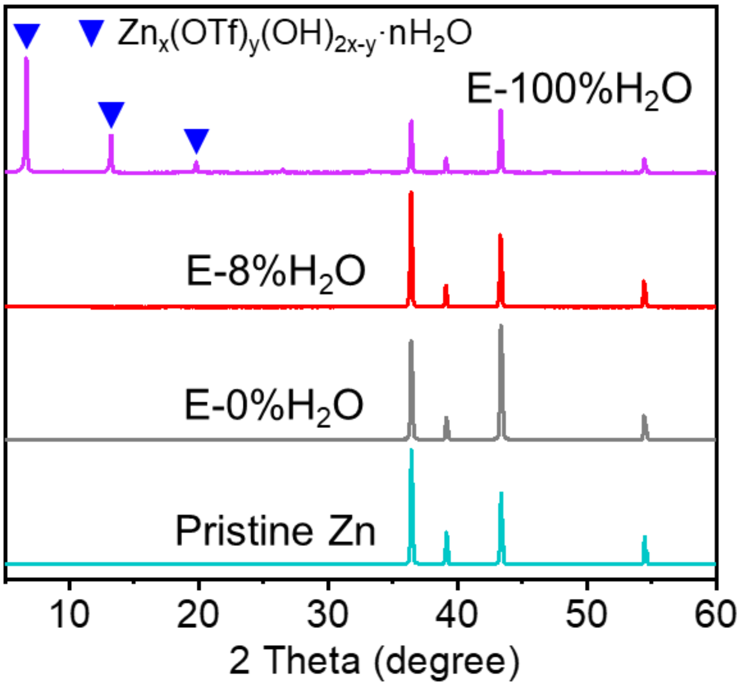

Fig. S20 XRD patterns of the Zn anode in the pristine state and after cycling in electrolytes with various water contents.

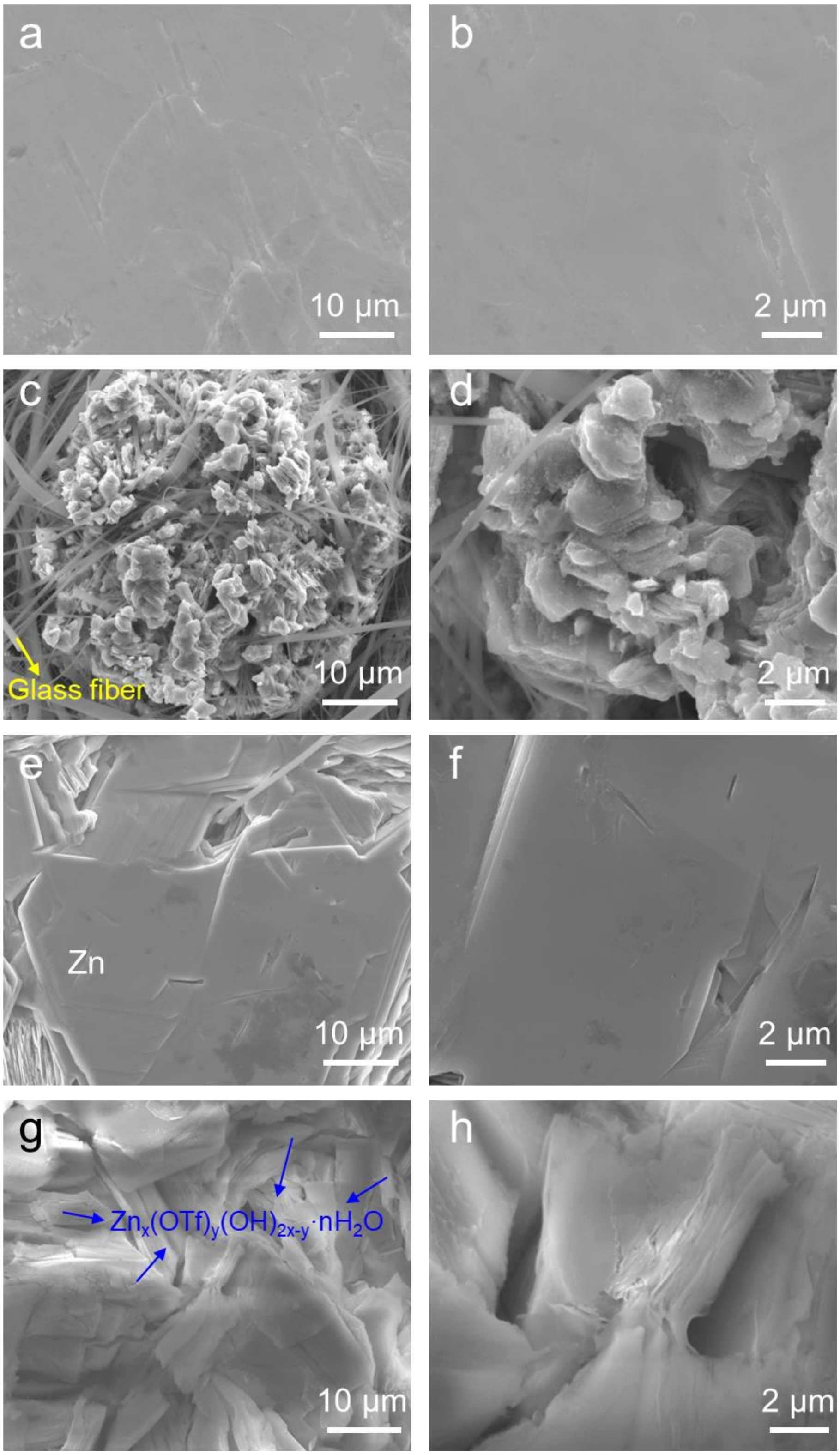

Fig. S21 SEM images of the Zn anode in the pristine state (a, b) and after cycling in electrolytes with various water contents (Fig. 4d): (c, d) E-0% H_2O, (e, f) E-8% H_2O, and (g, h) E-100% H_2O.

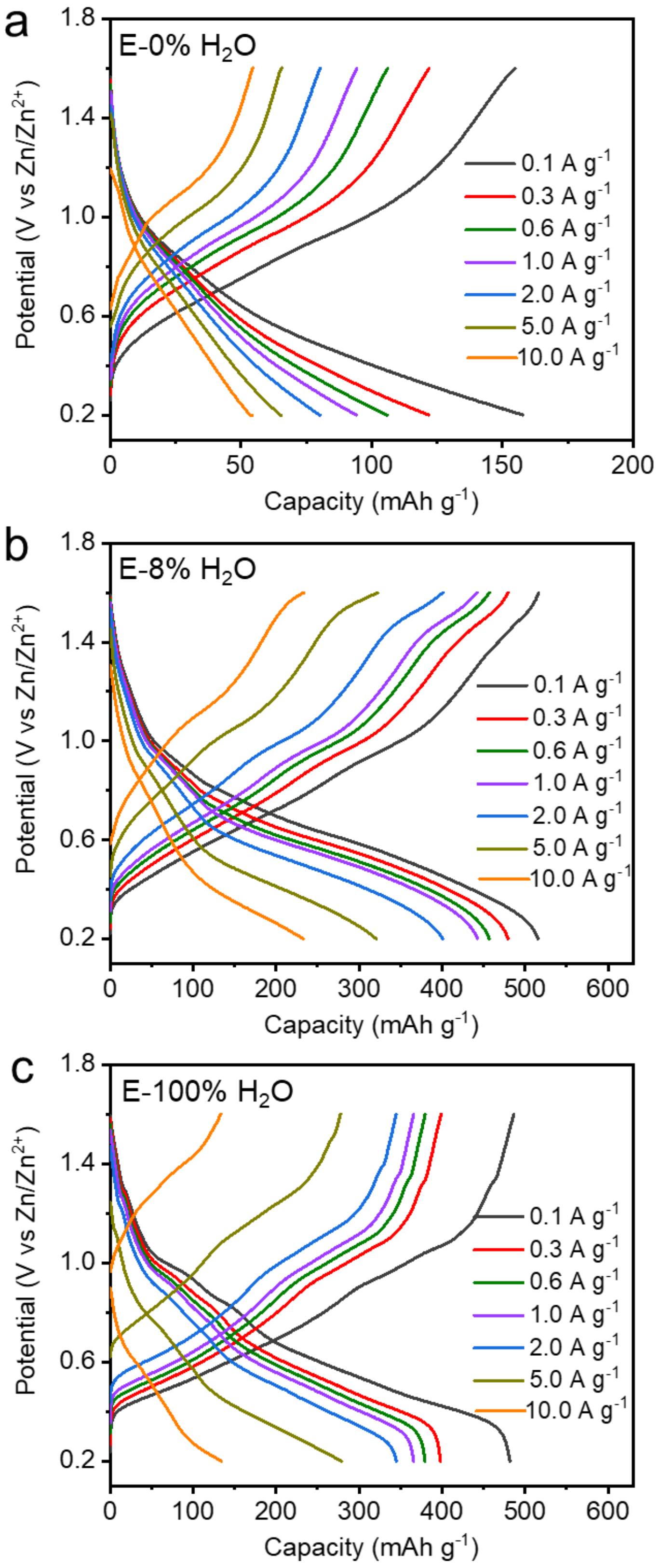

Fig. S22 Galvanostatic discharge/charge curves at different current densities for Zn||NVO cells in various electrolytes: (a) E-0% H_2O, (b) E-8% H_2O, and (c) E-100% H_2O.

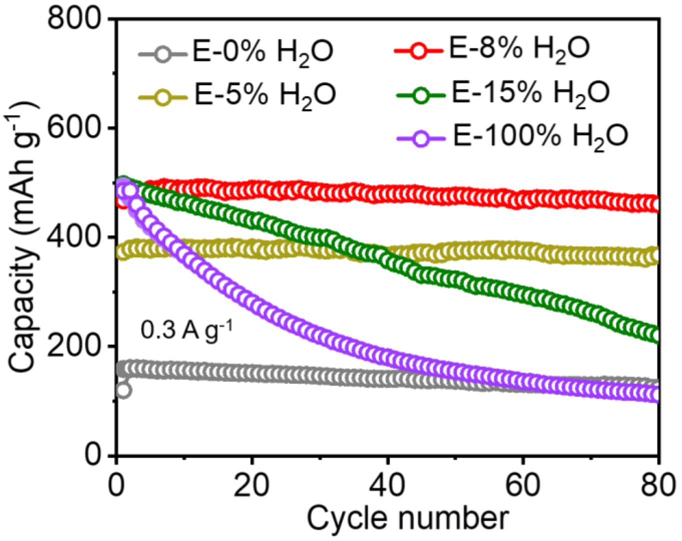

Fig. S23 Cycling performance at a current density of 0.3 A g^{-1} for Zn||NVO in electrolytes with various water contents.

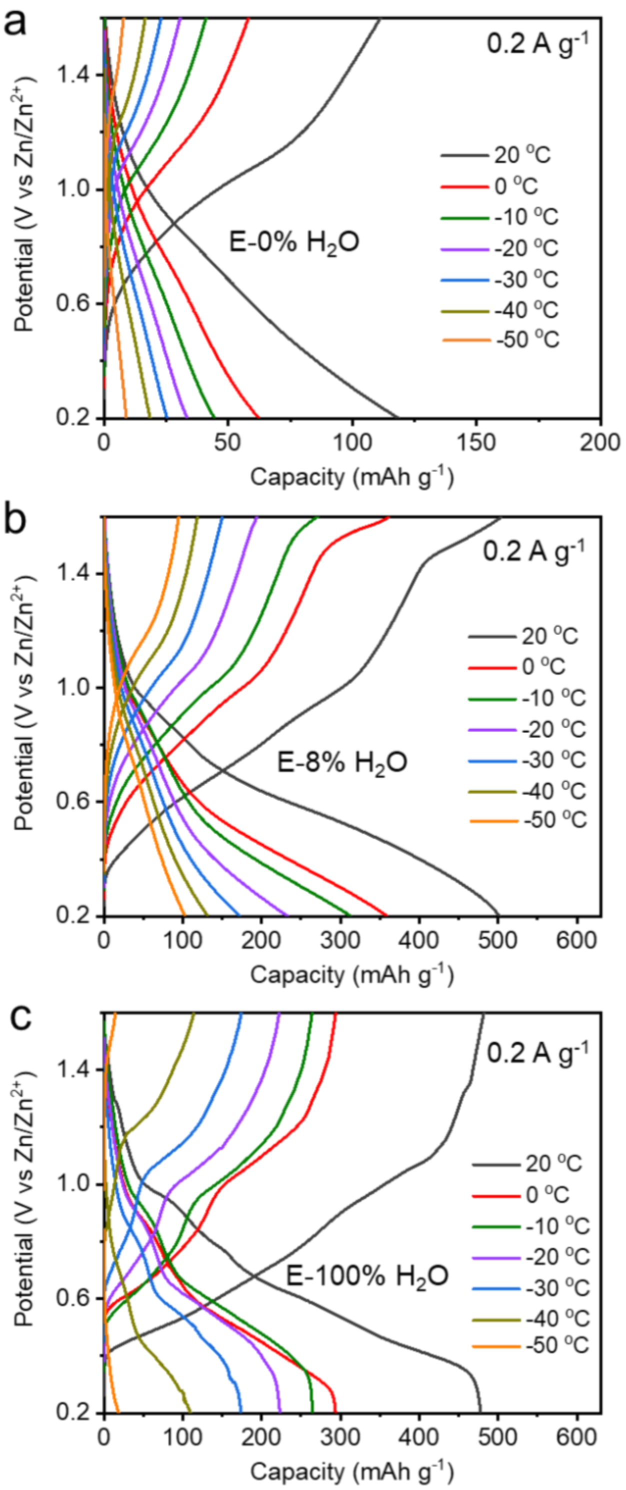

Fig. S24 Galvanostatic discharge/charge curves (0.2 A g^{-1}) at different temperatures for Zn||NVO cells in various electrolytes: (a) E-0% H_2O, (b) E-8% H_2O, and (c) E-100% H_2O.

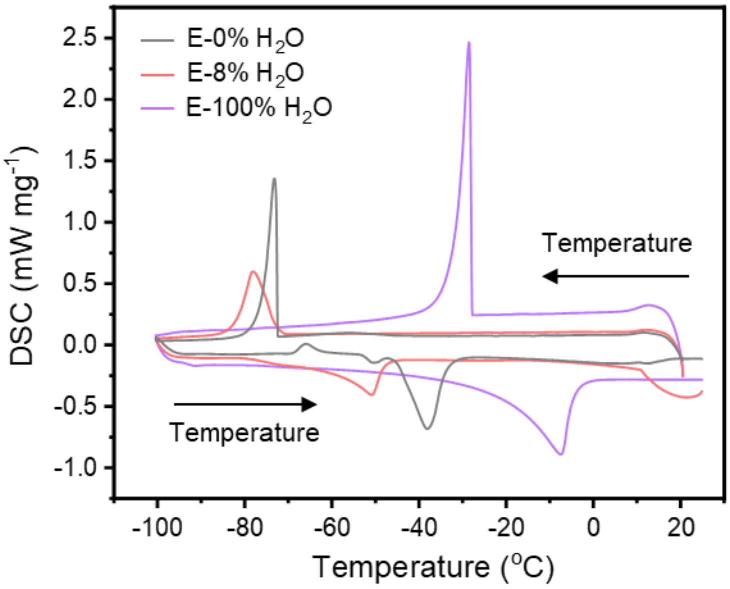

Fig. S25 Differential scanning calorimetry (DSC) curves of E-0% H_2O, E-8% H_2O and E-100% H_2O.

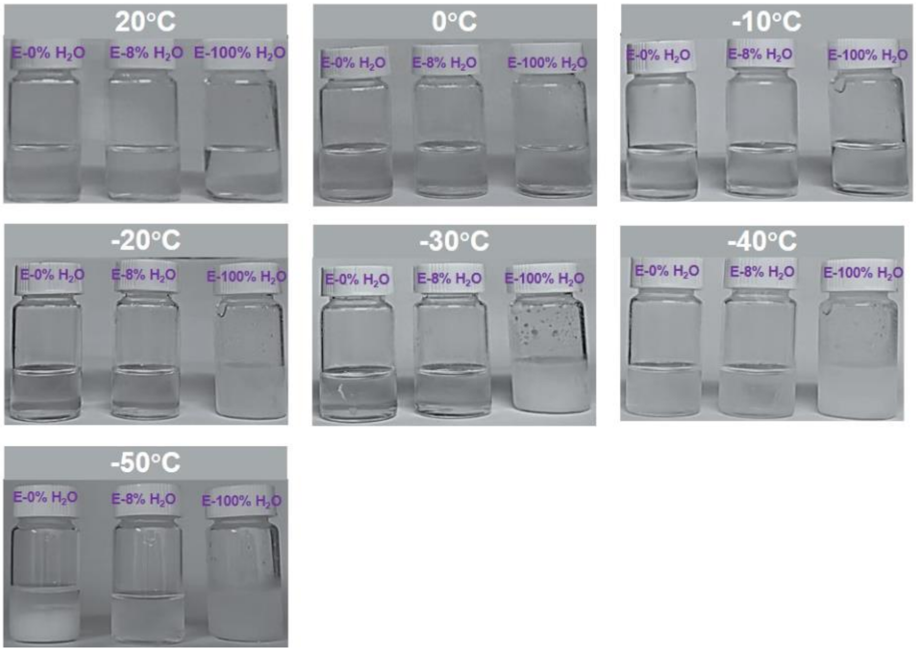

Fig. S26 Optical images depicting E-0% H_2O, E-8% H_2O, and E-100% H_2O at various temperatures.

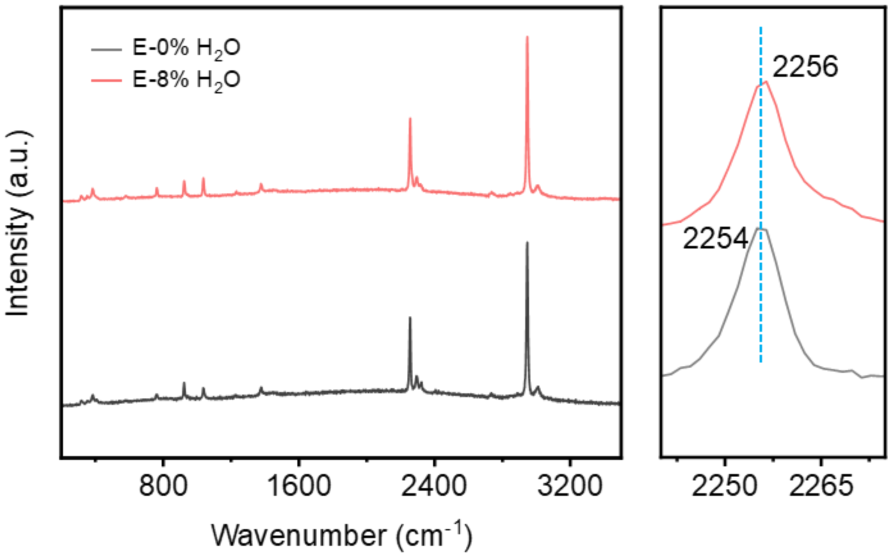

Fig. S27 Raman spectra of E-0% H_2O and E-8% H_2O.

Compared to that of E-0% H_2O, the blueshift of the peak at 2254 cm^{-1}, corresponding to the strength vibration of -C≡N, indicates the formation of hydrogen bonds between AN and water.[15]

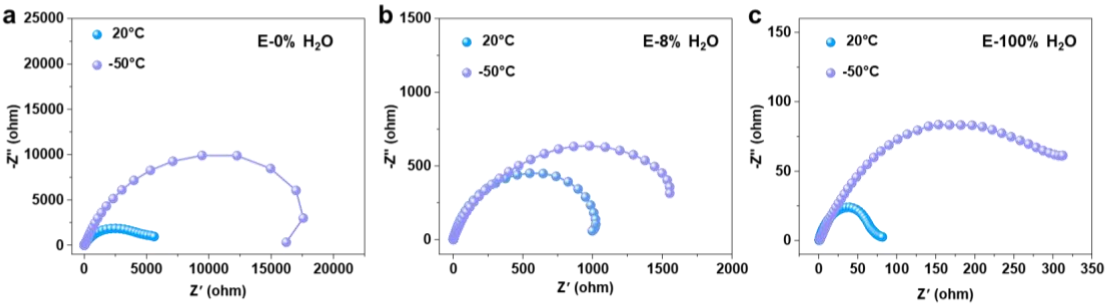

Fig. S28 EIS spectra at the OCV at 20 and -50°C for Zn||NVO cells in electrolytes of (a) E-0% H_2O, (b) E-8% H_2O and (c) E-100% H_2O.

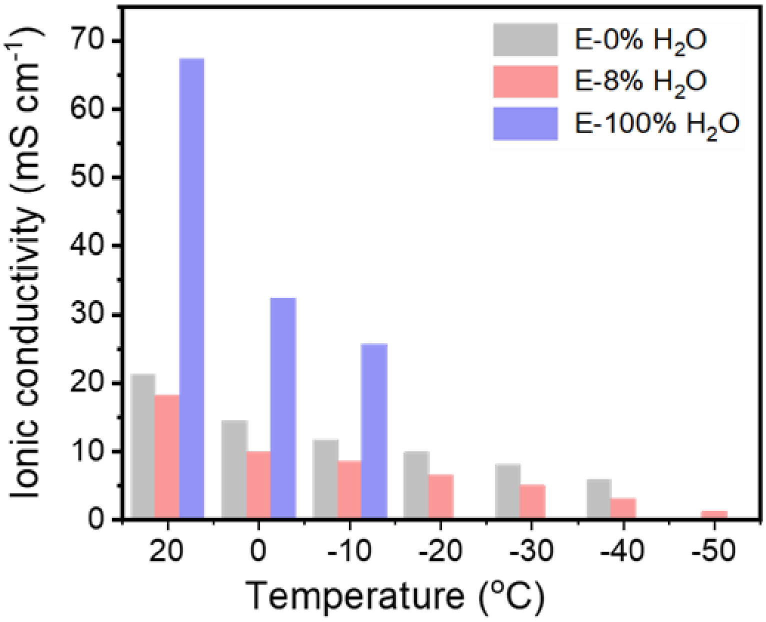

Fig. S29 Ionic conductivities of E-0% H_2O, E-8% H_2O, and E-100% H_2O at different temperatures.

The ionic conductivities of the electrolytes (E-0% H_2O, E-8% H_2O, and E-100% H_2O) were measured at various temperatures using a conductivity meter (DDBJ-350F, LEICI). As shown in Fig. S29, the ionic conductivity of E-100%H_2O decreases from 67.4 mS cm^{-1} to 25.6 mS cm^{-1} as the temperature drops from 20°C to -10°C. Although crystallization becomes apparent at -20°C in the E-100% H_2O electrolyte, complete solidification of the electrolyte solution does not occur at -30°C or -40°C. This explains why batteries using E-100% H_2O can still work at -40°C but fail at -50°C. On the other hand, the ionic conductivity of E-0%H_2O decreased from 21.3 mS cm^{-1} to 5.8 mS cm^{-1} as the temperature decreased from 20°C to -40°C, and an apparent salt-out phenomenon occurred at -50°C in the E-0% H_2O electrolyte. In contrast, the ionic conductivity of E-8%H_2O decreases from 18.2 mS cm^{-1} to 1.3 mS cm^{-1} as the temperature decreases from 20°C to -50°C.

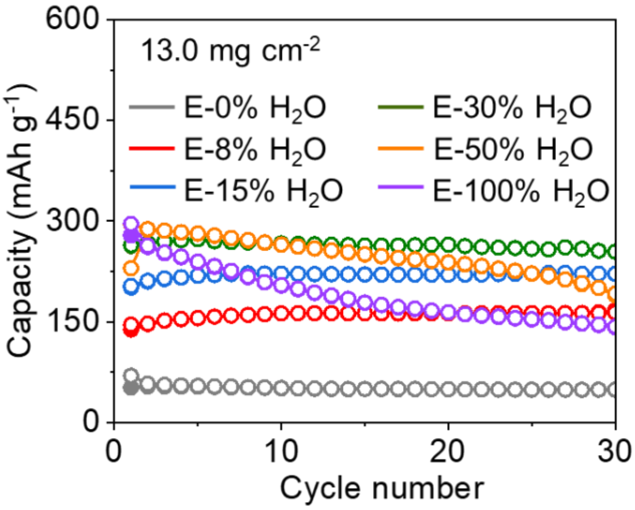

Fig. S30 Cycling performance (specific capacity based on active mass) at 0.5 A g^{-1} for Zn||NVO with an NVO mass loading of ~13.0 mg cm^{-2} in electrolytes with various water contents.

References:

(1) X. Guo, G. Fang, W. Zhang, J. Zhou, L. Shan, L. Wang, C. Wang, T. Lin, Y. Tang, S. Liang, *Adv. Energy Mater.*, 2018, **8**, 1801819.
(2) J. P. Perdew, Y. Wang, *Phys. Rev. B*, 1992, **46**, 12947–12954.
(3) C. Sosa, C. Lee, *J. Chem. Phys.*, 1993, **98**, 8004–8011.
(4) A. D. Becke, *J. Chem. Phys.*, 1992, **97**, 9173–9177.
(5) A. D. McLean, G. S. Chandler, *J. Chem. Phys.*, 1980, **72**, 5639–5648.
(6) R. Krishnan, J. S. Binkley, R. Seeger, J. A. People, *J. Chem. Phys.*, 1980, **72**, 650–654.
(7) H. J. Berendsen, D. van der Spoel, R. van Drunen, *Comput. Phys. Commun.*, 1995, **91**, 43–56.
(8) Y. Duan, C. Wu, S. Chowdhury, M. C. Lee, G. Xiong, W. Zhang, R. Yang, P. Cieplak, R. Luo, T. Lee, J. Caldwell, J. Wang, P. Kollman, *J. Comput. Chem.*, 2003, **24**, 1999–2012.
(9) S. Izadi, R. Anandakrishnan, A.V. Onufriev, *J. Phys. Chem. Lett.*, 2014, **5**, 3863–3871.
(10) T. Lu, Sobtop, Version [1.0], http://sobereva.com/soft/Sobtop.
(11) C. I. Bayly, P. Cieplak, W. Cornell, P. A. Kollman, *J. Phys. Chem.*, 1993, **97**, 10269−10280.
(12) T. -C. Liu, W. G. Pell, B. E. Conway, S. L. Roberson, *J. Electrochem. Soc.*, 1998, **145**, 1882.
(13) J. Wang, J. Polleux, J. Lim, B. Dun, *J. Phys. Chem. C*, 2007, **111**,14925-14931.
(14) V. Augustyn, P. Simon, B. Dunn, *Energy Environ. Sci.*, 2014, **7**, 1597-1614.
(15) W. Chen, S. Guo, L. Qin, L. Li, X. Cao, J. Zhou, Z. Luo, G. Fang, S. Liang, *Adv. Funct. Mater.*, 2022, **32**, 2112609.